New Chapter IV-B-2 in CRC Press Book Entitled
"Oceanographic Applications of Remote Sensing" - (Ed's) Ikeda, M. and Dobson, F.

APPLICATIONS OF SAR MEASUREMENTS IN OCEAN-ICE-ATMOSPHERE INTERACTION STUDIES

Mark R. Drinkwater
Jet Propulsion Laboratory
California Institute of Technology
4800 Oak Grove Drive
Pasadena CA 91109

a. INTRODUCTION

b. RESOLUTION AND COVERAGE ISSUES

    i, Temporal and Spatial Resolution
    ii. Spatial Coverage

c* COUPLED DATA AND MODEL APPROACHES

    i. Wind-Driven Ice Motion and the Momentum Balance
    ii. SAR and Ice-ocean Model Surface Flux Estimates
        Coupling SAR Observations and Physical Ice Growth Models
        Time-Series Backscatter Data and the Energy Budget

d. CONCLUSIONS

c* ACKNOWLEDGEMENTS

f. BIBLIOGRAPHY

g. TABLES

h. FIGURES

a. INTRODUCTION

The difficulty in observing the polar sea-ice cover and its influence on the atmospheric and oceanic boundary layer is the ephemerality of active geophysical processes. Identifying timescales of sea-ice formation, change and decay, is the key to successful measurement of these processes, Sea ice continuously adjusts to the ocean and atmosphere, and the magnitude or scale of corresponding changes is determined by the atmospheric and oceanographic forcing terms ranging spatially from meters to thousands of kilometers, and temporally from diurnal to decadal. Table I indicates the spatial and temporal scales of key sea-ice variables of interest to sea-ice geophysicists and oceanographers.

A conventional concern of high latitude oceanographers is that information gathered from space is not as accurate or as relevant as that collected first hand from research vessels or *in situ* by moorings or drifters. However, microwave radar imaging of sea ice is a young and evolving field, just as acoustic tomography and acoustic Doppler current profiling once were. SAR is an ideal candidate for monitoring sea-ice surface characteristics on a variety of time and space scales. Currently operating satellites with SAR will be succeeded for at least another decade by a new generation of approved instruments (see Appendix E). This will provide more than 10 years of continuous and almost unrestricted high-resolution imaging.

Traditionally ice extent is regarded as the parameter which microwave techniques can most successfully measure (Table I). This is done routinely by passive microwave instruments such as SSM/I which frequently map large areas (see section IV-A-2). Additional capability offered by higher resolution SAR (~ 30 m) is that individual features such as ice floes and leads can be tracked and monitored in space in time-sequential images. This capability is reviewed in [1] and the ability of the ERS-1 SAR to monitor patterns of ice motion and circulation in the Beaufort Sea is demonstrated, Algorithms measuring ice motion in satellite images similar to those described in section IV-B-1 enable routine motion measurements in areas such as the Fram, Denmark, and the Bering Straits. Whereas ice motion in these areas is too vigorous for buoys to be efficient or cost-effective, SAR images can provide new data on the Arctic freshwater balance by measuring ice mass flux through these regions. Equally important is the contribution of SAR to observing dynamics of leads and thin ice areas. SAR images acquired at intervals of several days enable changes in thin ice area to be quantified in relation to the motion field and spatial variations in velocity of ice floes. As subsequent sections show, when this information is coupled with physical models of ice growth and with air temperature and wind data, observations of divergence and thin ice formation in leads and polynyas can be employed in estimates of the

brine flux or salt precipitation rate in the upper ocean. Models can be exploited to estimate the sensible and latent heat fluxes, and with sufficient coverage and frequency, enable regional heat budgets to be monitored. With combinations of these measurements and data from judiciously placed buoys, SAR will make significant contributions towards assimilating information on variables in Table 1,

Experiments described in section IV-A-3 provided a wealth of airborne microwave signature data, Images acquired in conjunction with surface measurements provide the raw material with which to realize the potential of contemporary satellite SAR data, The main problem now facing polar oceanographers and sea-ice geophysicists is how to translate the knowledge gained from these SAR experiments into methods of extracting useful information from satellite systems. This section outlines some new applications of SAR ice-motion and surface characteristics data in geophysical process studies,

b. RESOLU'I'1ON AND COVERAGE ISSUES

Of the historical spaceborne SAR'S described in Appendix E, the Shuttle Imaging Radar (SIR) Space-Shuttle payload is the only spaceborne sensor other than Seasat SAR to recover sea-ice data between 1978 and 1991. It recorded only limited amounts of imagery of marginal ice in the Southern Ocean during the SIR-B mission in 1984 [2]. Its follow-on SIR-C mission, slated for launches in 1994, will also have low orbit inclination and therefore recover limited sea-ice data unless coinciding with maximum Southern Ocean ice extent, Of the ongoing satellite missions, ERS- 1 (and J-ERS-1) SAR data currently are of most practical use in geophysical studies. These have provided a largely uninterrupted data stream, and are recording considerable amounts of SAR image data of sea ice. In this section the impact of the resolution and coverage of these systems is investigated with respect to scientific investigations. Further information about present and future microwave instruments collecting sea-ice data is given by [3, 4] and the operating characteristics of each of these instruments are further described in detail in Appendix E.

A major difference between satellite and airborne systems is their inherent revisit capability and imaging swath width. Within range, an aircraft can revisit a surface site many times offering high spatial and temporal resolution, while the polar-orbiting ERS- 1 satellite SAR achieves nominally 3 days revisit with a small fraction of the earth visited at 1 day intervals [5]. Conversely, the satellite has an indefinite revisit (over long timescales of months to years) and greater spatial coverage, but with slightly reduced spatial resolution, Each of these approaches has its drawbacks, and more often than not there is a tradeoff. However, the solution to many of these

problems is to have a steerable SAR antenna on a satellite platform The SCANSAR mode which Radarsat offers will solve many of these difficulties (see Appendix E).

i. Temporal and Spatial Resolution

The capability to 'revisit' or repeat an image of an area on the ground has an impact upon the regional monitoring of lead areas or motion-induced divergence in the ice cover, Aliasing of observations of the areal extent of open water and thin ice is a topic of considerable interest to recovering information about the salt flux and heat exchange between ocean and atmosphere. Is a repeat cycle of three days sufficiently high temporal resolution to monitor the process of new ice formation in leads for instance? It is clear that the exact date of lead opening is critical for a number of reasons. Primarily ice growth is most vigorous during the early growth phase, throughout the period of the largest ocean-atmosphere heat exchange. Furthermore, concomitant salt fluxes during this phase are significantly higher and thus knowledge of the age of a lead is essential to understanding the impact upon the upper ocean. Equally importantly, the SAR repeat period is critical to observing seasonal ice zone features, as the timescales of features in the marginal ice zone are susceptible to rapid changes in thermodynamic and dynamic forcing. Consequently, repeat periods of 3 days, typical for ERS- 1 SAR, are unsuitable for some MIZ monitoring and most applications must rely on snap-shot images.

Orbits with longer repeat cycles often have sub-repeat cycles allowing imaging of a similar area on the ground at shorter intervals. Processing orbits such as that of the 35-day repeat orbit phase of ERS - 1, allowed 3-day repeat imaging and tracking of an moving patch of sea-ice over a longer period, provided that ice motion was westward and consistent with the precession of the orbit and that ice floes and features within the swath are larger than the resolution limit, Problems only occur in (i) regions where the circulation patterns dictate that the main velocity vector component is in a direction opposite to the orbit precession; and (ii) in marginal ice zones where ice drift velocities exceed around 0.6 m/s. Under these circumstances it is impossible to track the ice over long time periods and distances.

Spatial resolution in SAR data is superior to most alternative data sources and is sufficient for most applications except special cases found in marginal ice zones. Ice-floe tracking becomes almost impossible when floes decrease below the resolving power of the sensor and ice concentrations are high [6]. In spite of the problematic tracking, some information may be drawn from the patterns formed by the modulation of backscatter due to floe size or floe edge distributions. Increasing spatial resolution in order to solve these problems is a thorny issue,

because while limiting the study of marginal ice zones and narrow features such as leads, data volumes are already at a level which makes image products unwieldy. Studies have shown that for the majority of cases ice pack monitoring can successfully utilize low 100 m resolution images, Such is the case that all Alaska SAR Facility image post processing to ice motion velocity fields and ice type grids is currently performed on 100 m degraded resolution image data. The only short-term solution to improving upon 30 m satellite SAR resolution in seasonal ice zones is to use higher resolution aircraft SAR.

ii. Spatial Coverage

Satellite SAR has a large advantage over aircraft data when it comes to applications of the data requiring monitoring of processes responding to synoptic scale ocean and atmosphere dynamics. A typical 100 km swath from a satellite data is sufficient to conduct mesoscale or regional studies, and contiguous image strips can be used to trace events over wide areas in the along-track direction. In some cases it is impossible to monitor ice motion orthogonal to the swath and in the wrong direction (counter to orbit precession). The latter problem may be overcome by a SAR system with the flexibility to image much wider areas. Radarsat is capable of imaging a 510 km swath (see Appendix E), and offers the geographic coverage required to enable complete mapping of the Northern and Southern Hemisphere ice covers in 2 days (with a possible repeat only every 6 days - due to data volume). Only then will it be possible to track parcels of sea ice indefinitely in space and time, or indeed throughout an entire ice season. The capability of RADARSAT to image expansive areas on a weekly basis goes a long way to solving most of the problems associated with applying SAR data to geophysical problems. An additional feature which allows variable viewing geometry using multiple beams will enable beam steering to overcome the difficulties of ice monitoring in problematic regions of ice contraflow or particularly dynamic ice margins.

c. COUPLED DATA AND MODEL APPROACHES

i. Wind-Driven Ice Motion and the Momentum Balance

One important geophysical question is how sea ice responds to forcing from above and beneath by winds and currents, as the transfer of momentum to the sea ice is critical to understanding sea ice dynamics. This argument may be extended to the way ice motion responds to local winds causing discontinuous ice motion or divergence and the formation of leads. A major uncertainty in calculations of regional air-sea-ice heat exchange is the rate of ice divergence,

In this section pairs of Antarctic ERS-1 synthetic aperture radar (SAR) images are coupled with data from Argos buoy data to derive the ice kinematics and divergence in response to the surface wind forcing, The current state of the art in routine post-processing of image data allows tracking of sea ice features. Geophysical data products generated at the Alaska SAR Facility through the Geophysical Processor System (GPS) are; (i) ice motion vector fields, made from pairs of images separated by a few days in time from successive passes over the same ice; and (ii) ice classification images [7, 8] and an example illustrating these products from the Beaufort Sea is shown in Fig. 1. The motion field may be used simply to generate a deformation field in which the gridded relative displacements can be used to measure divergence or convergence in the ice together with the spatial derivatives in the x and y image directions. This approach is currently being extended at JPL to ERS-1 data products recorded for Antarctic ice. An example of a GPS ice motion product is shown in Fig. 2 for a pair of images located near to a drifting Argos buoy.

In the unenclosed Weddell Sea, Antarctica, ice motion is less affected by internal stresses generated by coastal contact. In situations away from the coast under largely divergent conditions, one may assume that the mean ice motion $\overline{\mathbf{v}}_i$ is steady and in balance with the mean current $\overline{\mathbf{c}}_i$ and the mean geostrophic wind $\overline{\mathbf{U}}_g$

$$\overline{\mathbf{v}}_i - \mathbf{A}\overline{\mathbf{U}}_g - \overline{\mathbf{c}}_i = 0. \tag{1}$$

A simple relationship then exists between the instantaneous time-varying part of the ice velocity $\mathbf{v}'_i$ and the instantaneous geostrophic wind $\mathbf{U}'_g$ [1]

$$\mathbf{v}'_i = \mathbf{A}\mathbf{U}'_g + \mathbf{e} \tag{2}$$

where the error term e contains all error sources including time-varying current and the divergence in the internal ice stress tensor. Importantly, the mean error term $\overline{\mathbf{e}}$ is zero which accounts for its absence in Eq. (1). Matrix A in each case may be considered as a complex scale factor (lAl, δ) with the real part lAl giving the magnitude of the ratio of ice speed to wind speed, and the imaginary part δ the rotation or turning angle (positive = clockwise) between the ice and the wind vectors. Similar schemes have recently been used to explain the drift of sea ice in the Weddell Sea [9, 10].

Under divergent conditions, a free-drift form of the ice momentum balance can successfully be used to simulate Eastern Weddell Sea ice drift, with some assumptions regarding ice-water drag and internal ice stress [11]. To-date this approach has been used for two separate buoy drift experiments to derive the typical range of winter Antarctic 10 m neutral drag coefficients [9, 11],

In 80-100% concentration ice they observed air-ice values in the range 1.45 x $10^{-3} \leq C_{dn10} \leq$ 1.79 x 10-3 with aerodynamic roughnesses spanning $0.27 \leq z_0 \leq 0.47$ mm, and derived a value for the ice-ocean drag coefficient of 1.13 x 10⁻3.

Data reported on here characterizes ice motion in the Eastern-Central Weddell Gyro in an area of Argos drifters deployed by the Germans from the research vessel Polarstern in July 1992 during the Winter Weddell Gyre Study (WWGS '92). Figure 2 indicates selected results from these SAR images and six buoys placed in the Central Weddell Gyre. In Fig. 2a the position of two geolocated ERS-1 SAR images are shown with respect to the July portion of the drift track of Buoy 6. In Fig. 2b the corresponding SAR-tracked ice motion is shown for a 1 day time period between this pair of images acquired on 13 and 14 July. In Fig. 3a the daily mean drift distance and 24 h smoothed velocity of Buoy 6 indicates the response to pulses in the geostrophic wind U_g' (calculated from the two-dimensional buoy pressure-gradient field) as it drifts along the track depicted in Fig. 2a. The corresponding response of the area encompassed by a triplet of Argos buoys (including Buoy 6) to U_g' is equally sensitive, This area shown in Fig. 3b increases consistently over the month of July in response to the wind stress, and the fractional area of new ice production in this period is 1100 km^2, equating to a mean divergence of 0.67 ± 0.45 %/day. Sea ice quickly reacts to pulses in geostrophic wind, as shown in the 24-hr smoothed divergence in Fig. 3b. Each pulse of relatively stronger winds is interleaved by relaxation events where the ice pack converges and leads close under internal stresses. In contrast, divergence over the whole six-buoy array in July results in a mean value of 0.4 ± 0.6 %/day. Southeastern buoys tend to converge over the same July period and spatial variability in the divergence results in a lower mean and larger variance than that represented in Fig. 3b. This spatial variability in divergence on different scales makes it imperative that the satellite data are additionally employed in monitoring regional divergence and hence region-wide new ice production.

The ice motion derived from the SAR motion field in Fig. 2b indicate a mean ice motion vector magnitude Vi of 0.255 m/s, with a bearing θ_i of 17.466° (when the vectors are correctly referenced to the Southern Hemisphere SSM/I grid by a 45° rotation). The mean geostrophic wind $\overline{U_g}$ over the same period is 6.3 m/s, on a bearing of 36.5°. Preliminary results comparing these buoy-derived winds with the first Antarctic ERS-1 SAR-derived ice motion give values for (1A1, δ) of (0.04 , -190). The turning angle is consistent with a mean of $|A| = 0.03$ and $\delta = -20°$ (to the left of the wind) observed during periods of free drift during W WGS '86 and '89 [11].

Further processing of SAR ice motion data acquired during WWGS '92 will form an Antarctic satellite ice-motion database for comparison with buoy statistics of velocity and divergence. The

tested relationships between wind-stress and divergence, under essentially free-drift conditions, can also then be extended to yield similar bulk drag coefficients through this simple formulation of the momentum balance, In addition more accurate long-term measurements of divergence can be made in order to make estimates of the impact upon heat exchange between the upper ocean and atmosphere.

ii. SAR and Ice-ocean Model Surface Flux Estimates

Coupling SAR observations and Physical Ice Growth Models

A simple extension can be made of the results shown in Fig. 2 by coupling the regional SAR-derived divergence measurements with an ice growth model. In Fig. 4a the full energy balance is computed using longwave radiation (LW) budget and short-wave (SW) fluxes (from WWGS '92 shipborne measurements) and estimates of the turbulent fluxes of sensible (SH) and latent heat (LH) driven by the mean surface geostrophic wind speed values plotted in Fig. 3. The energy balance is then used in a coupled two-dimensional ice growth model (extended from [12]) to simulate growth of an ice sheet (Fig. 4b) and the conductive heat flux (F_{COND}) for the month described by the buoy drift and SAR motion data. Typical snow data are added in the model to reproduce observed natural conditions and with uninterrupted growth the ice sheet reaches a thickness of 55 cm in only 16 days. Figure 4b indicates salinity and temperature profiles of this ice sheet at 10 cm growth-thickness intervals. Corresponding brine volume profiles are computed as a direct input to backscattering models which require vertical profiles of dielectric properties within the ice sheet. The direct relevance of this technique for oceanography, however, is shown in Fig. 4c and 4d, where the impact upon the upper ocean is monitored by calculating the flux of salt from ice to upper ocean as brine rejection and drainage take place. During early growth, when the air temperatures were close to -30°C, winds of between 4 and 10 m/s combine to cause a net outgoing heat flux of around -100 W/m^2. With clear skies and relatively brisk winds the sensible heat flux drives a net heat flux (F_{NET}) which on Day 205 reaches -300 W/m^2. Resulting ice growth is rapid with the first day growth rate peaking at 15 cm/d. After this early peak the rate slows to more typical values of 2 cm/day. A similar trend is seen in the salt flux data (Fig. 4d) whereat peak growth the salt flux exceeds 65 $kg/m^2/month$.

This brief example continues from the theme developed using the buoy and ice motion data. Future SAR measurements of regional ice divergence and the fraction of open water, together with a physical ice growth model such as that presented here, will enable the regional heat and salt budgets of such experiment areas to be assessed.

Time-series Backscatter Data and the Energy Budget

A further extension to our understanding of microwave backscattering response from sea ice can also be drawn from studying radar backscatter time-series in conjunction with this ice modelling and radiation balance approach. In this example a time-series of surface C-band scatterometer measurements is shown during a 3 day Weddell Sea ice drift station at the end of the month of July when the net heat flux budget shows a dramatic transition [13]. Field experiment data from WWGS '92 for a 1 m thick ice sheet in Fig. 5 records 10 minute averages of wind stress and turbulent sensible heat flux together with the net energy budget (courtesy of W. Frieden of Hannover University, Germany) during a C-band radar scatterometer time-series of measurements between days 203 and 206 (21 to 24 July, 1992). In the lowermost panel of Fig. 5 the 45° incidence C-band signature is plotted starting at Julian Day 203.79. The solid line with error bars represents the mean vv-polarized backscatter and the dashed line the corresponding hv polarized backscatter. A 10 dB variation in vv polarized backscatter (σ^{o}_{vv}) and 5 dB variation in hv polarized backscatter (σ^{o}_{hv}) is observed in response to the changes in the heat fluxes presented.

Fig. 5a indicates a large variation in wind stress during this period, increasing rapidly to over 0.5 N/m^2 when the winds peaked at 20 m/s. The increase in wind took place with a sudden rise in air temperature (Fig. 5b) from around -23°C to O"C during the passage of a warm frontal system. As a consequence of the overcast skies, warm temperatures and the high wind, the sonic-anemometer-thermometer recorded a net negative (downward/incoming) flux of sensible heat which peaked during the strong winds at 60 W/m^2. A sharp decrease in the amount of incoming turbulent sensible heat occurs on the morning of 24 July, due to the clear night sky.

A net energy budget (F_{NET}) is shown in Fig. 5c as a solid line, using the conventional system of negative net outgoing flux of heat and positive net incoming heat flux. The largest measured components of this budget are indicated as; the net radiative flux (Q); the net sensible heat flux (H); and the conductive heat flux (F_{COND}). At the start of the period, the surface lost nearly 50 W/m^2 in radiative and sensible heat with this loss balanced largely by conducted heat. Some heat is supplied by the freezing at the base of the ice sheet, as indicated by ice core measurements and a thermistor chain frozen into the sea ice. Immediately the sky became overcast on day 204 temperatures rise and light snowfall began. Several dB variability in backscatter (Fig. 5d) indicates several orders of magnitude change in backscattering over the conditions indicated during the following period. The change in heat flux regime is strongly correlated with a reduction in vv and hv backscatter as the net radiative and sensible heat flux (Q+H) swings from outgoing to incoming. At first conduction takes care of the surface warming, carrying heat away

from the snow and ice surface until the time at which the ice sheet becomes nearly isothermal (at day 205.5). Melting then begins to wet the snow surface and the backscatter rapidly rises to its peak. Subsequently, high winds and a brief period of cloud-free night at Julian Day 206.25 encourage evaporative cooling, a minimum in F_{NET}, and a local minimum in the values of vv and hv-pol backscatter.

Surface measurements in association with the C-band radar data indicate that the vv-polarized data clearly signal the change in heat flux environment when air temperatures rise above -20°C. While surface temperatures rose dramatically, snow-grain transformations began and equi-temperature metamorphism is first focused at the surface reducing the large angular grains to small rounded grains. As the warm temperatures penetrate down to the ice surface the previously exaggerated snow temperature gradients become reduced. However, the wind speed continues to rise to gale force. The σ^o_{vv} reduction mirrors the rise in Q+H in Fig. 2c, reaching a minimum below -35 dB. A reversal then occurs in σ^o_{vv} with a rise in backscatter values up to a level higher than that on day 203. During this period, no significant amount of surface wetness accumulated in the shallow 3 cm deep snow layer until the latter part of day 205. Instead, the wind speeds at the surface were large enough that sufficient heat is removed by surface sublimation to prevent visible melting and free- water appearance in the snow (as described in [14]), Until after day 205.5, it is suggested that in the case of these strong winds enough heat is removed by sublimation and conduction to preclude significant melting. The large change in thermal profile in the snow rapidly changed snow crystal characteristics under these conditions from hoar-style angular crystals (induced earlier by strong negative heat gradients before day 204) to rounded crystals. Together with the layering which developed in the snow, it is proposed that these snow changes play a large role first by reducing and then subsequently by increasing volume scatter as rounded grains grow larger. The last significant change in σ^o_{vv} takes place after cooling and overnight refreezing (day 206) of moisture in the snow layer upon a brief reversal of the net heat budget from positive to negative. Diurnal cooling and the swing in the humidity during this period on day 206 result in a brief minima in σ^o_{vv}. The rapid return to values above -30 dB coincide with the brief period of incoming short-wave energy during scattered clouds at mid-day and signifies the reappearance of moisture at the surface of the snow.

This winter example clearly indicates that the sea-ice surface properties respond to the balance of fluxes at the surface. Furthermore, C-band values of σ^o_{vv} react equally sensitively to these changes. Though these temperature swings may be more commonly associated with spring conditions, this change in events may be recognized in time-series data to reflect transformations in the surface heat and vapour flux environment. It is proposed that with the aid of buoy data and

weather analysis fields (for specifying boundary conditions), satellite SAR and surface data be used together with physical models to understand how microwave data reflect key changes in the energy balance. The power of time-series measurements using SAR backscatter has barely been exploited. Coupling data analyses in this manner together with the tracking capability of SAR provides a powerful method for studying geophysical processes and surface changes.

do CONCLUSIONS

SAR is now guiding us to geophysical variability previously unrecognised by way of the resolution and the time dimension often absent in sampling of polar geophysical media because of the logistical difficulty of routine observations. The goal of future satellite datasets therefore shall be to provide both a Lagrangian time-series of the characteristics and dynamics of sea ice floes tracked across the Arctic basin or Southern Ocean. Parcels of sea ice can already be followed through their evolution from thin new ice to multiyear ice using a Lagrangian style sea-ice tracker. This requires observations be frequent, continuous and indefinite over a large geographic expanse. We are already close to this goal when Radarsat arrives with an existing mandate to map the complete sea-ice cover of both hemispheres once every week. Tracking a piece of ice throughout its lifetime negates the necessity to identify ice "types" -or indeed to use such ice categories as a proxy for sea-ice thickness. Having sufficient accompanying environmental information enables a physical ice-growth model to be coupled with the observed lifecycle of the ice in simulating true thickness. In this way, contiguous parcels of ice over extensive regions may be integrated into a regional ice thickness distribution.

The main problem confronting scientists wishing to exploit SAR remote sensing of the polar ice pack is coping with the vast amounts of data being recovered. Automated algorithms which are tested and validated must become the accepted norm, and are a necessary step to digesting the spatial and temporal dimensions of the resulting datasets. The key to realising geophysical applications of these data is recognizing the requirement to process vast amounts of data routinely with knowledge of the errors inherent in the post-processing techniques used. Quantitative data can then be derived from these SAR products and used to reflect the changing surface characteristics of the sea-ice pack in response to the changing surface heat and salt flux environment.

e. ACKNOWLEDGEMENTS

f. BIBLIOGRAPHY

[1]　Holt, B. M., D.A. Rothrock, and R. Kwok, Determination of Sea Ice Motion from Satellite Images. In *Microwave Remote Sensing of Sea Ice,* Geophysical Monograph 68, Chapt. 18, American Geophysical Union, 343-354, 1992.

[2]　Martin, S., B. Holt, D.J. Cavalieri, and V. Squire, Shuttle imaging radar B (SIR-B) Weddell Sea ice observations: a comparison of SIR-B and scanning multichannel microwave radiometer sea ice concentrations, *J. Geophys. Res.,* 92, C7, 7173-7179, 1987.

[3]　Carsey, F.D., R.G. Barry, and W.F. Weeks, Introduction, *Microwave Remote Sensing of Sea ice,* Geophysical Monograph, 68, Chapt. 1, 1-7, 1992.

[4]　Massom, R., *Satellite Remote Sensing of Polar Regions,* CRC Press Inc., Boca Raton, FL 33431, 307pp., 1991,

[5]　ESA, ERS- 1 System, *ESA Special Publication,* SP-1 146, 87pp., 1992.

[6] Drinkwater, M.R., and V.A. Squire, C-band SAR observations of marginal ice zone rheology in the Labrador Sea, *IEEE Transactions on Geoscience and Remote Sensing,* 27, 5, 522-534, 1989.

[7] Kwok, R., J.C. Curlander, R. McConnell, and S.S. Pang, An Ice-Motion Tracking System at the Alaska SAR Facility, *IEEE Trans. Oceanic Eng., 15,44-54,* 1990.

[8] Kwok, R. E. Rignot, and B. Holt, Identification of Sea-Ice Types in Spaceborne Synthetic Aperture Radar Data, *J. Geophys. Res., 97, C2, 2391-2402, 1992,*

[9] Martinson, D. G., and C. Wamser, Ice drift and momentum exchange in winter Antarctic pack ice, *J. Geophys. Res., 95, 1741-1755, 1990.*

[10] Kottmeier, C, and D. Engelbart, Generation and atmospheric heat exchange of coastal poynyas in the Weddell Sea, *Boundary Layer Meteorology, 60,207-234, 1992.*

[11] Wamser, C., and D.G. Martinson, Drag coefficients for winter Antarctic pack ice, *Journal of Geophysical Research,* In press, 1993.

[12] Cox, G.F.N, and W.F. Weeks, profile Properties of Undeformed First-Year Sea Ice, CRREL Rep., 88-13, 57pp., 1988.

[13] Drinkwater, M. R., R. Hosseinmostafa, and W. Dierking, Winter Microwave Radar Scatterometer Sea Ice Observations in the Weddell Sea, Antarctica. *Proc. IGARSS '93,* Tokyo, Japan, Aug. 18-21, 1993.

[14] Andreas, E.L., and S.F. Ackley, On the differences in Ablation Seasons of Arctic and Antarctic Sea Ice, *J. Atmospheric Sci.*, *39,440-447, 1982.*

m

Table 1.   Sea ice variables of primary interest for atmosphere-ocean-ice interaction studies.

Parameter	Horizontal Spatial Scale	Temporal Scale	Accuracy
Ice Extent	100 m - 10 km	1 d - 10 y	< 0.1 % of area
Ice Thickness	O- 100 km	1 d - 7d	10 - 50 cm
Thin Ice Coverage	1 m - 10 km	1 h - 10 d	< 1% of area
Ice Divergence	1 -100,000 km2	1 - 7 d	< 1 % /d
Ice Type	10- 1000 km	7 d - 1 m	*(loo/# types)
Snow Depth	0 - 1 km	1 - 7 d	5 cm
Summer Melt	100-1 x 106km2	7 d - 6 m	570 of area
Meltponding (Albedo)	O- 10 km^2	7 d - 6 m	< 3 % of area
Ice Motion	0.1- 10 km	1 - 7 d	2 cm/s
Ice Growth Rate	0.1 - 10 km	1 h - 7 d	10 cm /d

Figure Captions

Figure 1. Example of geophysical products routinely generated at the Alaska SAR Facility from ERS- 1 SAR data (courtesy Ron Kwok and Ben Holt, JPL). Images were acquired 3 days apart in the Beaufort Sea in November 1991. The ice motion vector and deformation grids are shown in the centre panels with the classified images at-e shown in the lowermost panels.

Figure 2, Illustration of ice drift and deformation extracted from Antarctic FIRS-1 SAR images and an Argos drifter instrumented site in the central Weddell Sea, Antarctica. (a) Geolocated SAR image locations superimposed upon the July drift track of buoy 9364; (b) polar stereographicall y projected SAR image on 14 July, 1992 (Day 196) with superimposed vectors illustrating the ice motion field over a 24 hour period from day 195-196 [SAR image © ESA].

Figure 3. (a) Daily displacement and (b) drift speed of Antarctic Argos buoy 9364 in comparison with (c) geostrophic wind speed (Ug) in July 1992; (d) buoy triplet area change and (e) 3 hour] y divergences (points) superimposed by the smoothed mean daily divergence.

Figure 4. Radiation balance and new ice growth during July 1992, in the region around the buoy shown in Fig. 2. (a) Radiation balance of a newly opened lead; (b) ice properties during one month of new ice growth starting on day 193; (c) ice growth rate; and (d) the resulting salt flux over this period.

Figure 5. Shipborne C-band microwave radar scatterometer time-series comparison with surface fluxes of heat and momentum. (a) turbulent flux of momentum; (b) turbulent flux of sensible heat with the variation in air temperature and humidity; (c) the energy balance and its major components; and (d) 45° incidence vv- and hv-pol. backscatter response with temperature and air-surface temperature variations.
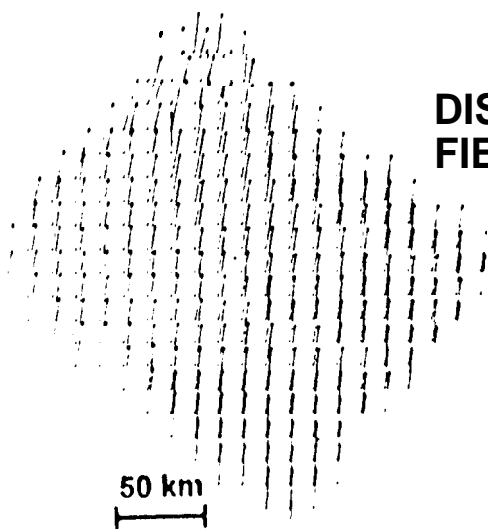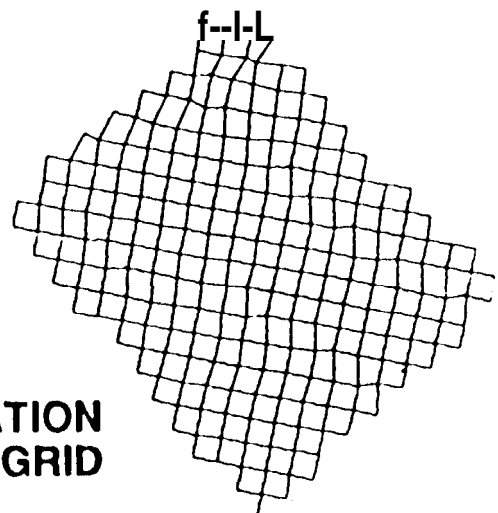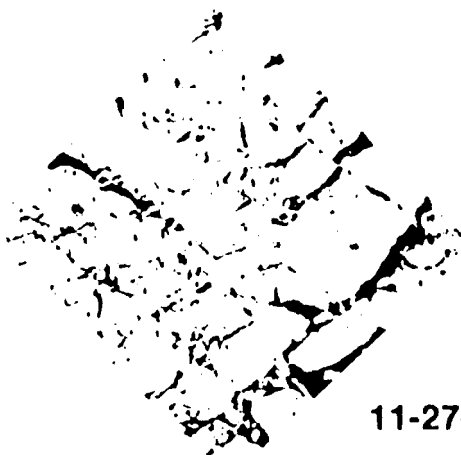
ERS-1 SAR IMAGERY
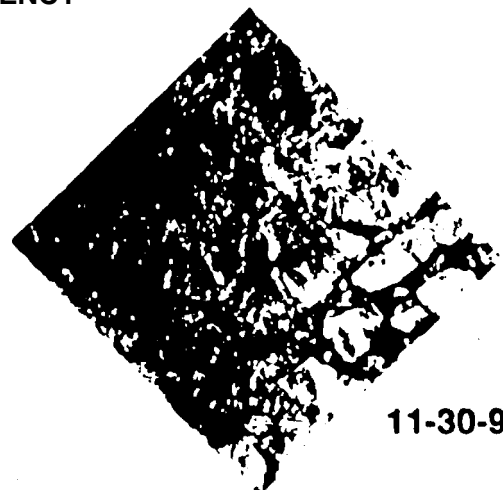
11-27-91

11-30-91

DISPLACEMENT FIELD

f--l-L

DEFORMATION GRID

50 km
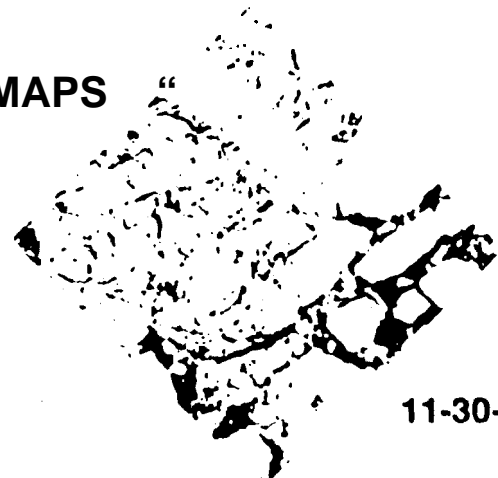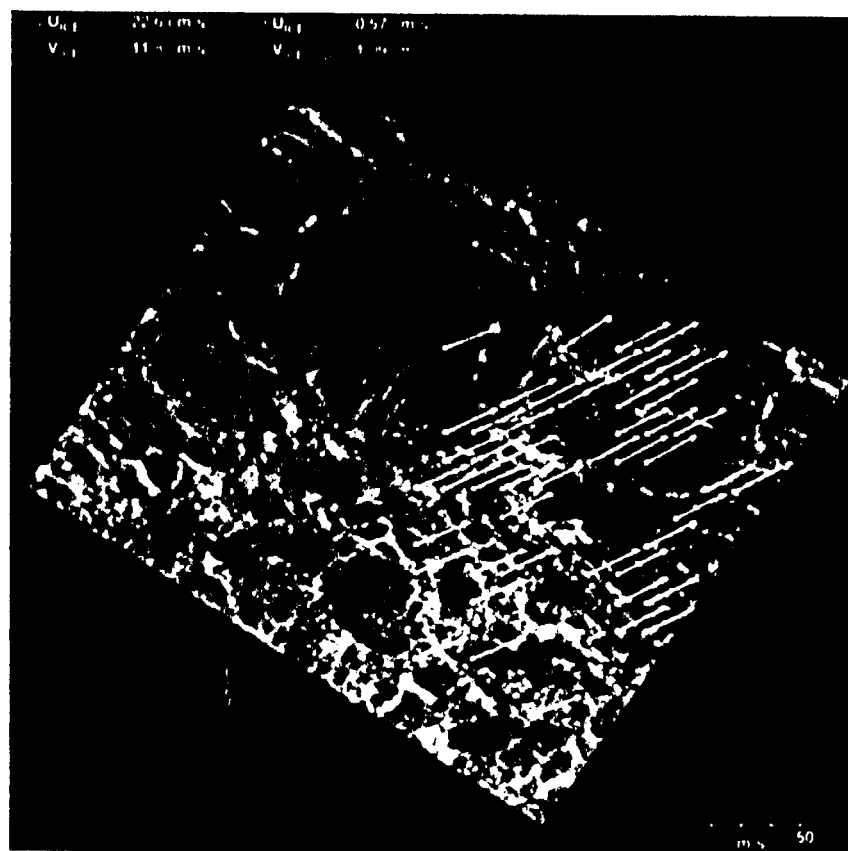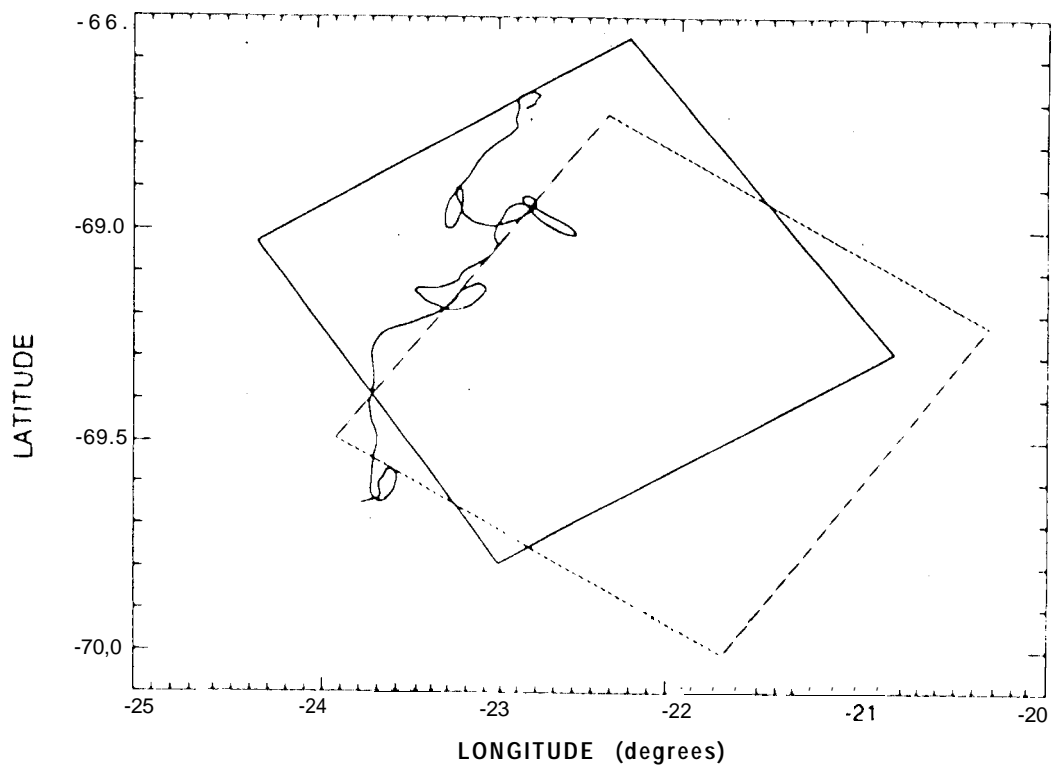
ICE TYPE MAPS

11-27-91

11-30-91

**MULTIYEAR ICE - WHITE, DEFORMED FIRST YEAR ICE – BLUE
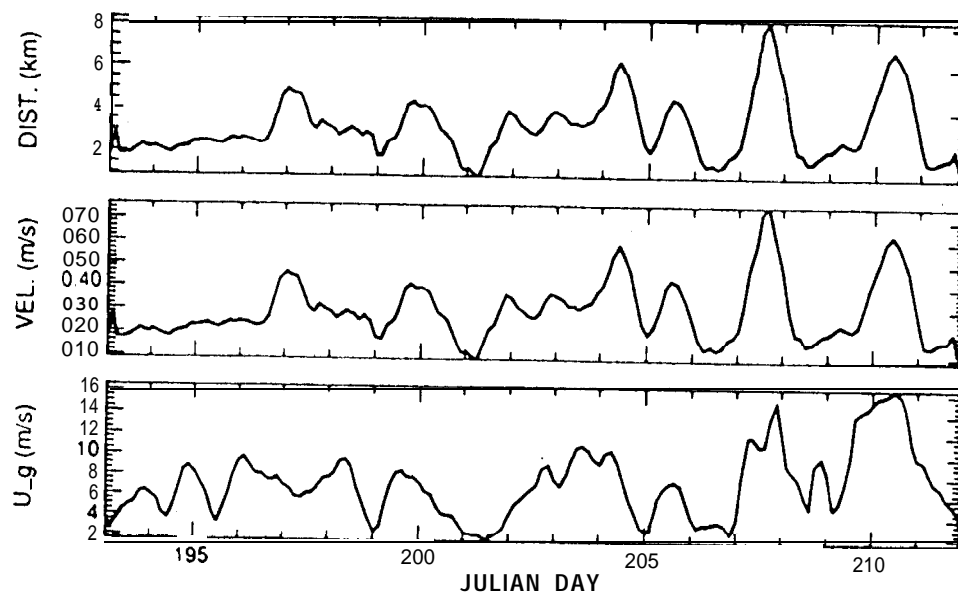UNDEFORMED FIRST YEAR ICE - GREEN, NEW/YOUNG ICE - RED**

FIG 1   FIG 1

(a)
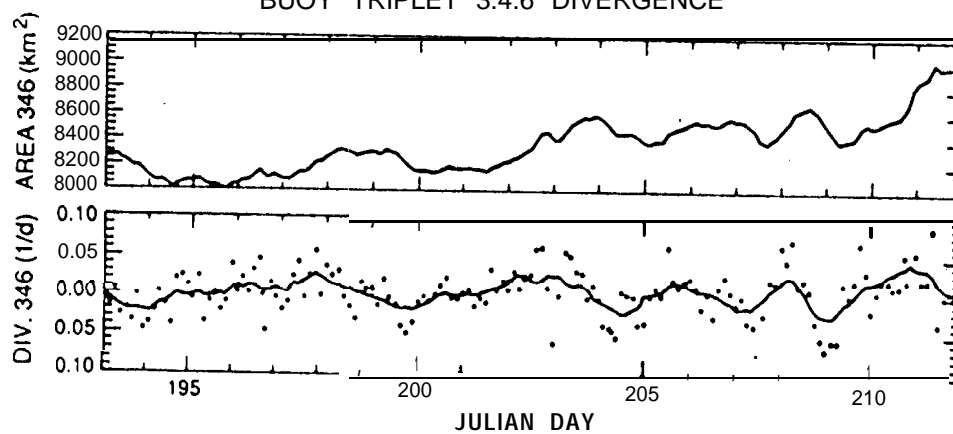
WWGS 92 BUOY 6 DRIFT

(b)

BUOY TRIPLET 3.4.6 DIVERGENCE

(a)

(b)

(c)

(d)

JULIAN DAY